

# Meshworm: A Peristaltic Soft Robot With Antagonistic Nickel Titanium Coil Actuators

Sangok Seok, Cagdas Denizel Onal, *Member, IEEE*, Kyu-Jin Cho, *Member, IEEE*, Robert J. Wood, Daniela Rus, *Fellow, IEEE*, and Sangbae Kim

**Abstract**—This paper presents the complete development and analysis of a soft robotic platform that exhibits peristaltic locomotion. The design principle is based on the antagonistic arrangement of circular and longitudinal muscle groups of *Oligochaetes*. Sequential antagonistic motion is achieved in a flexible braided mesh-tube structure using a nickel titanium (NiTi) coil actuators wrapped in a spiral pattern around the circumference. An enhanced theoretical model of the NiTi coil spring describes the combination of martensite deformation and spring elasticity as a function of geometry. A numerical model of the mesh structures reveals how peristaltic actuation induces robust locomotion and details the deformation by the contraction of circumferential NiTi actuators. Several peristaltic locomotion modes are modeled, tested, and compared on the basis of speed. Utilizing additional NiTi coils placed longitudinally, steering capabilities are incorporated. Proprioceptive potentiometers sense segment contraction, which enables the development of closed-loop controllers. Several appropriate control algorithms are designed and experimentally compared based on locomotion speed and energy consumption. The entire mechanical structure is made of flexible mesh materials and can withstand significant external impact during operation. This approach allows a completely soft robotic platform by employing a flexible control unit and energy sources.<sup>1</sup>

**Index Terms**—Bioinspired robotics, earthworm robot, nickel titanium (NiTi) coil springs, peristaltic locomotion, soft robotics, shape memory alloy (SMA) actuation.

## I. INTRODUCTION

IN the last several<sup>1</sup> decades, many robotics researchers have devoted themselves to develop soft robots inspired by biology [1], [2]. Soft robots are especially beneficial for delicate tasks, rough terrain negotiation, recovery from overturning, and safety in human interaction [3]. Developing soft actuators is one of the critical requirements to enable these structures.

Manuscript received March 28, 2012; accepted May 9, 2012. Recommended by Technical Editor Y. Sun. This work is supported in part by the Defense Advanced Research Projects Agency (DARPA) under Grant W911NF-08-C-0060 (Chemical Robots).

S. Seok and S. Kim are with the Department of Mechanical Engineering, Massachusetts Institute of Technology, Cambridge, MA 02139 USA (e-mail: sangok@mit.edu; sangbae@mit.edu).

C. D. Onal and D. Rus are with the Computer Science and Artificial Intelligence Laboratory, Massachusetts Institute of Technology, Cambridge, MA 02139 USA (e-mail: cagdas@csail.mit.edu; rus@csail.mit.edu).

K. J. Cho is with the School of Mechanical and Aerospace Engineering, Seoul National University, Seoul 151-742, Korea (e-mail: kjcho@snu.ac.kr).

R. J. Wood is with the School of Engineering and Applied Sciences, Harvard University, Cambridge, MA 02138 USA (e-mail: rjwood@eecs.harvard.edu).

Color versions of one or more of the figures in this paper are available online at <http://ieeexplore.ieee.org>.

Digital Object Identifier 10.1109/TMECH.2012.2204070

<sup>1</sup>Some material in this paper has been adapted from two papers: [4] and [5]

Several soft actuators such as ionic polymer metal composite (IPMC), electroactive polymers (EAP), nickel titanium (NiTi) shape memory alloy (SMA) wires, and springs are proposed. IPMC actuators are light and enable large bending displacements, but can generate only a small force. EAPs generate large deformations, but generally require a large electric field and rigid frame structure, with a small force output as well. SMA actuators are able to generate large displacements with simple mechanisms. They, however, exhibit slow cycle frequencies due to the passive cooling on the restoration phase [6]. Even so, SMA spring actuators have a extremely large energy density per cycle (1314 J/kg) [4] and are promising for soft robots with modest speed requirements.

Many soft-bodied animals such as earthworms, sea cucumbers, snails that use peristalsis for locomotion provide inspiration for soft robotic platforms [7]. There are several benefits of the combination of a soft body with peristaltic locomotion. A soft body, which is essentially compliant, exhibits large strains [1] and enables the robot to traverse small openings and reconstitute shape, and survives from large impact force on falling. Peristaltic locomotion is slow but stable locomotion alternative [8] with reduced noise generation and also requires a smaller form-factor than legged or wheeled locomotion [9].

Due to these benefits, several soft-bodied robotic peristaltic locomotion platforms have been developed for confined space such as endoscopy or reconnaissance purposes. In [10], a flexible endoscope is developed. This device uses balloons and extensors that vary their length alternately to achieve peristaltic motion. Likewise, Mangan *et al.* developed serial segmented pneumatic actuators, which create peristaltic locomotion of an endoscope [11]. Another work utilized rubber cells filled with a water-based magnetic fluid instead of pneumatic actuators. These cells expand sequentially by an external moving magnetic field to generate peristaltic locomotion [9]. On the other hand, Kim *et al.* developed a capsule endoscope with a directional frictional skin, actuated by piezoelectricity, which creates reciprocal motion of two halves [12]. The authors later replaced the actuation mechanism to SMA springs in [6]. Similarly, longitudinal SMA spring actuators were used to actuate multiple elastic segments in [13], where the stored elastic energy in the segments extends the structure. Recently, large scale peristaltic locomotion has been demonstrated by a cylindrical robot with a braided mesh body made of brake cable sheathing, which has steel cables wrapped around. A single-cam mechanism on one end of the body creates traveling waves along the length of the robot by applying tension on the steel cables [14].

Our approach to develop a soft worm-like crawling robot enables many new features in comparison to the state of the

art. In the literature, similar robotic systems typically utilize rigid mechanical components. The sizes of these components are significantly large, which limits the deformability of the body. Meshworm, the subject of this paper, utilizes flexible mechanical components in its mechanism for actuation. The only rigid parts on the body are electrical in nature: a battery and a printed circuit board. Having a flexible mechanical body and no rigid transmission elements reduces limitations on the size of the robot, making it more compact. Additionally, as rigid mechanical components are more prone to failure upon impact, our robot is safer.

In this paper, we describe an entirely soft mobile robotic platform that exhibits peristaltic locomotion. The robot utilizes coiled NiTi fibrillar actuators. It consists of a series of segments that contract to induce peristalsis. We achieve steering by additional longitudinal actuators that contract to bend the tubular body in an intended direction. Iterative learning control (ILC) algorithms regulate the contraction period of each segment to optimize underlying objective functions of performance.

The contributions of this study are as follows.

- 1) Modeling, design, fabrication, and evaluation of NiTi SMA coils as artificial muscle fibers.
- 2) Development of a soft mobile robot, tagged the Meshworm, consisting of multiple contractile segments undergoing peristaltic crawling locomotion.
- 3) Development of control algorithms realize optimized performance and steering.

The organization of this paper is as follows. Section II investigates coil NiTi wires used as compact fibrillar actuator. We model and identify parameters to tune the behavior of these actuators. In Section III, we present a peristaltic soft mobile robot inspired by earthworm locomotion observed in nature. We outline basic locomotion principles of this robot, using sequential contraction of multiple NiTi coils wound around the cylindrical body. In Section IV, we develop ILC algorithms using various objective function to optimize the performance of the robot. Section V discusses the addition of longitudinal actuator fibers to implement steering.

## II. NiTi COIL ACTUATORS AS MICROARTIFICIAL MUSCLE FIBERS

NiTi) is one of the well-known SMA materials that generate mechanical work by phase change. Despite its low efficiency, it has a high energy density, which gives the ability to develop relatively small scale actuators compared to other types of actuators mentioned in Section I. In a solid state phase transformation, the crystal structure of the NiTi compound transforms from martensite to austenite states with up to 7% strain change [15]. For larger displacements, coiled spring NiTi wires can be used.

Various NiTi models suggested from the 1990s are discussed in [16]. These are mostly thermodynamic models of various forms of NiTi such as wires, tubes, and sheets. Coiled spring NiTi models were discussed in [6], and [17]–[19]. These models, however, are relatively incomplete. The existing models focus on the mechanical coiled spring equations using different shear moduli for the martensite and austenite phases, overlooking the

change in the free length of the spring due to the phase transition. A more appropriate model, which is useful for a design of coiled spring NiTi is proposed in Section II-A. This model combines the mechanical and thermodynamic aspects of NiTi coil actuators to describe the overall martensite deformation and the geometrical spring effect together. We use this model as a guideline for actuator design for the Meshworm robot.

There are two major steps to fabricate NiTi coil springs. First, an NiTi wire is wound around a straight core, and then the coiled NiTi wire is annealed at a certain high temperature in order to reset the memorized shape as a spring. During the annealing process, mechanical properties and the actuation performance of NiTi springs are determined by the annealing temperature. In Section II-B, the manufacturing process is detailed and experimental data between deflection and force under various annealing temperatures are presented.

### A. Modeling of NiTi Coil Actuators

Even though NiTi spring actuators are widely used [6], [17]–[19], complete design models have not been developed yet. Recent works utilize the mechanical coiled spring equation with two shear moduli,  $G_M$  and  $G_A$  which are the martensite and austenite phases, respectively. However, none of these models consider the free length change of the NiTi spring due to phase change. The free length of 100% austenite phase  $x_{Ao}$  is shorter than the free length of 100% martensite  $x_{Mo}$ .

There are two major physical phenomena in NiTi coil spring deformation. One is the free length change due to the phase transformation explained earlier, and the other is the spring constant difference between the martensite and austenite states. The spring constant in the austenite phase is around 2–3 times greater than in the martensite phase [16].

Fig. 1 shows five typical states of an NiTi coil spring during actuation. When the NiTi coil is heated up above the phase transition temperature, it becomes austenite and fully contracts as in Fig. 1(a). If a load  $F$  is applied in this state, the spring will have a displacement  $\delta_H$  as shown in Fig. 1(b). When the temperature is below the transition temperature, it becomes martensite and the crystal structure of NiTi twins [20] without an observable overall shape change [see Fig. 1(c)]. If a load is applied below the transition temperature, the crystal structure is detwinned [20]. Fig. 1(e) shows the detwinned martensite with a load  $F$ , and Fig. 1(d) shows the detwinned martensite in free length after the detwinning load is removed. The free length difference between austenite and detwinned martensite is  $\delta_M$ . The displacement  $\delta_L$  is the length difference between loaded martensite and unloaded martensite under fully detwinned status.

In general, the NiTi spring actuation cycle starts in the martensite phase with an external load  $F$ . And then, the spring is activated by heating it up to transition temperature, which results in a spring length contraction under the load. The displacement created in this transformation is called effective displacement,  $\delta_{\text{effective}}$ , and calculated as follows:

$$\delta_{\text{effective}} = \delta_M + \delta_L - \delta_H. \quad (1)$$

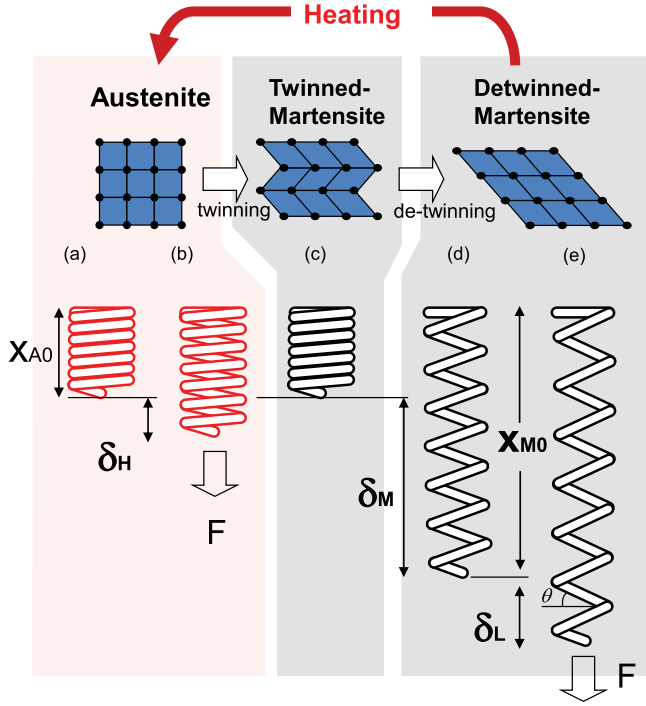


Fig. 1. Five representative states of an NiTi coil spring actuator: (a) full austenite without load, (b) full austenite with load, (c) twinned martensite without load, (d) fully detwinned martensite without load, and (e) fully detwinned martensite with load.

Here, each  $\delta_i$  value, where  $i \in \{H, L, M\}$ , corresponds to the displacement of the coil. Using the general coiled spring deflection equation,  $\delta_i$  is a function of an external load  $F$ , overall spring diameter  $D$ , NiTi wire diameter  $d$ , number of active coils in the spring  $n$ , and the shear modulus of the spring after annealing  $G$

$$\delta_i = \frac{8FD^3n}{Gd^4}. \quad (2)$$

The shear strain  $\gamma$  of the spring is

$$\gamma = \frac{\tau}{G} \quad (3)$$

and the shear stress  $\tau$  is

$$\tau = \frac{8FD\kappa}{\pi d^3} \quad (4)$$

where  $\kappa$  is a stress correction factor. From Wahl's formula [21],  $\kappa$  is

$$\kappa = \frac{4C-1}{4C-4} + \frac{0.615}{C}. \quad (5)$$

Here  $C$  is the spring index, defined as follows:

$$C = \frac{D}{d}. \quad (6)$$

Using this analysis, the difference of the free length between the austenite and martensite phases  $\delta_M$  can be calculated from (2) through (4) as

$$\delta_M = \frac{\pi\gamma D^2n}{d\kappa}. \quad (7)$$

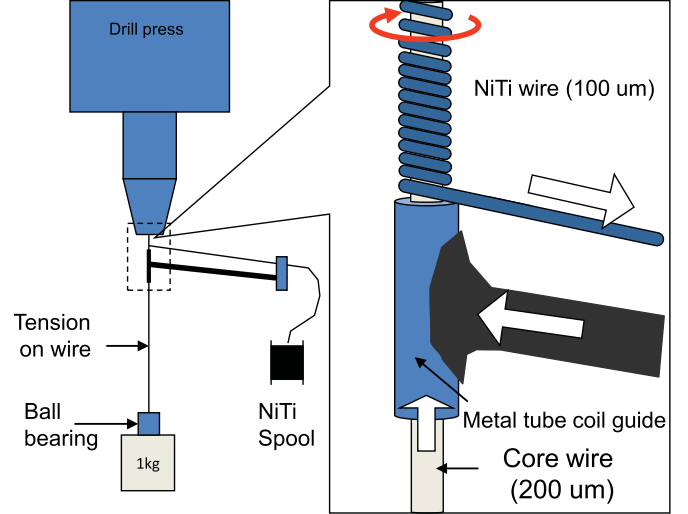


Fig. 2. Simple manufacturing system enables the fabrication of long strand coiled springs of NiTi muscle fiber. The core wire is under tension and an NiTi wire is wound around the core. The guidance tube is slightly larger than the core wire. The tension of the NiTi wire is maintained by friction between NiTi and the long bar.

Therefore, for a given  $F$ , the effective displacement from (1) is given as follows:

$$\delta_{\text{effective}} = \frac{\pi\gamma D^2n}{d\kappa} + \frac{8FD_{\text{eff}}^3n}{G_M d^4} - \frac{8FD^3n}{G_A d^4}. \quad (8)$$

There is a significant coil diameter  $D$  change when the coil spring is elongated under martensite phase with a load  $F$ . Therefore, to calculate the displacement properly in this situation, an effective spring diameter  $D_{\text{eff}}$  is used

$$D_{\text{eff}} = D \cos \theta \quad (9)$$

where  $\theta$  is the angle between the spring wire and the horizontal plane.

### B. Fabrication and Characterization of NiTi Coil Actuators

Our fabrication process of micro-NiTi coil muscle fibers is depicted schematically in Fig. 2. One end of a 200- $\mu\text{m}$  diameter core wire and a 100- $\mu\text{m}$  diameter NiTi wire [Dynalloy Flexinol (R)] are clamped at a drill press. Constant tension is applied to the core wire by attaching a weight on the free end. A metal tube and a bar attached to the tube make up the coil guide, which is essential for closely packing the NiTi coil on the core. The friction of the metal tube on the core acts against the tension from the coiled NiTi and keeps the core wire vertical.

After winding the NiTi to a given length, the ends of the coil are clamped to the core wire and annealed in an oven under a controlled temperature. The annealing temperature determines various parameters of the resulting spring actuator. Two noticeable trends are identified that vary with the annealing temperature: 1) increasing the annealing temperature decreases the detwinning force, and 2) large annealing temperatures cause the resulting springs to lose their ability to return to their original dimensions after loading.

Detwinning is a passive process that returns the actuated NiTi coils in the twinned martensite state back to the fully detwinned martensite state through martensite transformation. This requires external work, such that a certain amount of tensile force pulls the coils to extend them, transforming their state in the process. This force is strongly dependant on the annealing temperature, and is a mechanical characteristic of the actuators. When used in an antagonistic configuration, such that the actuation of one coil detwinds the other, this characteristic force requirement affects the full cycle work efficiency of the actuators.

We experimentally investigated the dependance of the detwinning force on the annealing temperature. 25-mm-long NiTi coil springs are annealed at nine different temperatures ranging from 300 °C to 540 °C in 30 °C increments. Weights are hanged on the coils to apply varying external forces. Weight application and removal were carried out slowly to reduce dynamic effects and the spring effect. The final elongated length was measured under no load, after the weights were removed.

Fig. 3(a) depicts the results. In these curves, detwinning is indicated as a plateau, similar to a plastic deformation behavior in stress-strain curves. The value at which this plateau occurs is the detwinning force. This force clearly decreases with the increasing annealing temperature as a general trend. After detwinning, the coils yield a larger stiffness, indicated by a sharp gradient in the curve after the plateau. This stiffness change occurs at larger deflections as the annealing temperature is increased. We used an annealing period of 20 min for these experiments. We found no change in actuator characteristics above this value.

The second effect of the annealing temperature on the NiTi coil actuator operation is shown in Fig. 3(b). This is a curve of permanent deformation of these actuators, 25 mm in original length, after lifting a 35-g weight only once. The permanent deformation is measured as the difference between the final length in the austenite state after lifting and the original length of the coils. The data indicate that springs annealed at a temperature below 400 °C show reasonable consistency at multiple trials. In contrast, springs annealed at higher temperatures yield large permanent deformations after multiple trials. In short, even though higher annealing temperatures result in smaller detwinning forces, the original dimension is lost for springs annealed above 400 °C after a single lifting cycle, a tradeoff in fabrication.

Based upon these observations, we used an NiTi coil spring annealed at 390 °C for further experiments. Weight lifting experiments are performed and stroke lengths are measured for comparison of the model output with experimental results. Fig. 3(c) displays our results of deflection of springs in both the austenite and the martensite states with various loads. We applied a constant current of 150 mA to maintain the spring in the austenite state under load. Model predictions from (2) are plotted with the experimental data. The shear modulus of NiTi is also a function of the annealing temperature. Thus, we calculated this value through the deflection length in the austenite state. As the martensite state shear modulus, we used a third of the austenite shear modulus, which is the typical case for NiTi [21].

The work done by the NiTi coil springs when they lift a known weight yields the energy density of these actuators. A

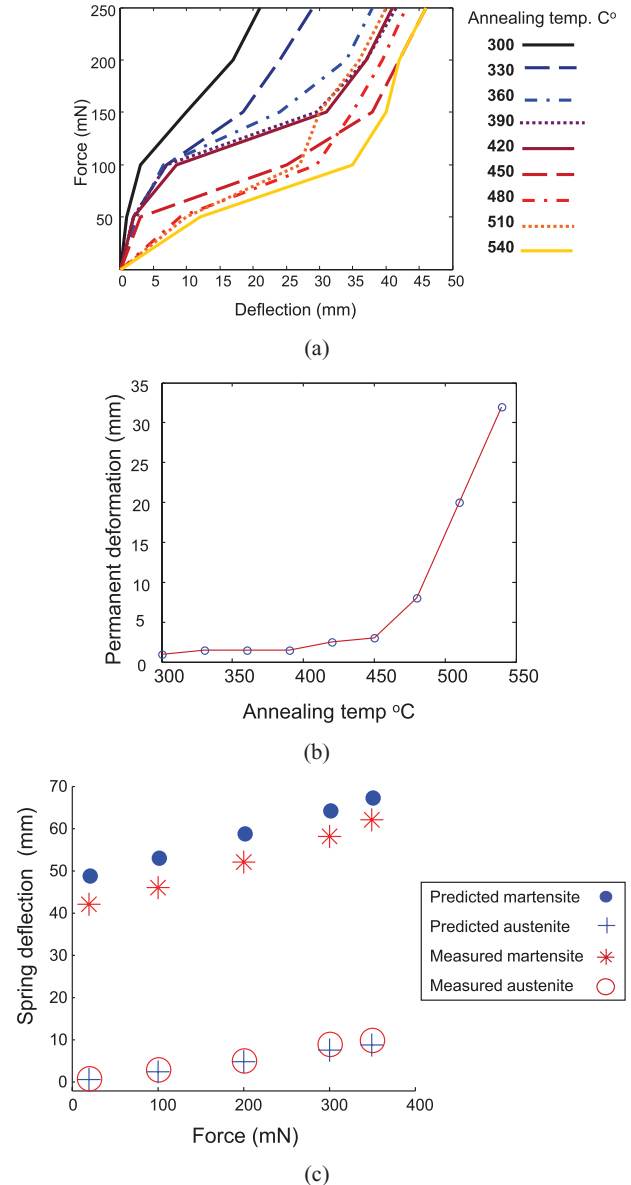


Fig. 3. Experimental results of NiTi coil spring. (a) Deflection of springs annealed at various temperatures under load. (b) Permanent plastic deformation of NiTi coil springs annealed at various temperatures, after lifting a 35-g weight. (c) Experimental NiTi coil spring deflection data are compared to the theoretical model predictions: Average errors in Martensite and Austenite phases are  $-22\%$  and  $12.4\%$ , respectively.

25 mm long NiTi coil annealed at 390 °C lifts a 37.9-g weight with a stroke length of 50 mm. The total energy to perform this task is then 0.0184 J. The weight of the NiTi coil is 0.014 g. Thus, the energy density, defined as the amount of work done by unit mass of this actuator in a single stroke, is calculated to be 1314 J/kg.

### III. PERISTALTIC LOCOMOTION OF A SOFT BRAIDED MESH BODY

Inspired by the hydrostatic skeletal structure of Oligochaeta, we present a novel antagonistic actuation mechanism utilizing the NiTi muscle fibers discussed in the previous section. A

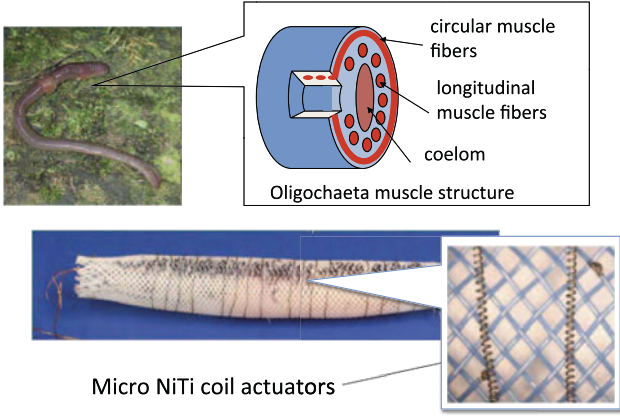


Fig. 4. Oligochaeta utilize antagonistic radial and longitudinal deformation of the body. The meshworm is a robotic prototype that exhibits peristaltic locomotion induced by a similar antagonistic configuration.

peristaltic crawling robot is created from a soft braided mesh-tube and NiTi coils, inspired by earthworm locomotion. This robot, called the Meshworm, can use its soft body to adapt and negotiate with rough terrain. Generating antagonistic actuation in a tubular soft structure, the robot can locomote using a peristaltic traveling wave along the length of its body from head to tail in a small form factor.

Limbless invertebrates such as Oligochaeta (worms) need to deform their body in order to generate the essential locomotion process of engagement, propulsion, and detachment. By deforming their body in a peristaltic wave pattern, worms modulate friction forces of ground contact points of the body. Especially for applications in limited space, peristalsis may allow robustness in locomotion without the complexity of limbs.

#### A. Antagonistic Actuation

Natural muscles operate only in contraction directly. Vertebrates achieve bidirectional motion by a kinematic arrangement of rigid bones, connected with joints, and contractile muscles antagonistically. Invertebrates utilize a hydrostatic skeleton for shape change and stiffness modulation. In particular, Oligochaeta employ an antagonistic coupling of radial and longitudinal muscles to contract and extend body segments. Fig. 4 shows the arrangement of muscle groups found in Oligochaeta.

In earthworms, coelom in each septum contains a liquid that acts as fluidic transmission between the radial and longitudinal directions. With this fluid-filled divided cavity, worm segment deformation follows a constant volume constraint [22], [23]. Thus, the hydrostatic skeleton can be considered as an elastic tube that varies its radius and length subject to a fixed internal volume. The hydrostatic bodies of earthworms are controlled by the antagonism between radial (or circular) and longitudinal muscles [23].

A similar antagonistic configuration is inherent in braided-mesh tubes [4]. The mesh is made of multiple spiral polymeric fibers woven into a tubular shape. As the length of a segment on the mesh is increased, the spiral pitch of the fibers also increases and the segment radius decreases accordingly. Similarly,

a decrease in length (and pitch) leads to radial expansion. In a constant volume cylinder, this relationship follows (10) and in a mesh-tube it is described by (11)

$$r^2 l = \text{Constant} \quad (10)$$

$$Ar^2 + l^2 = \text{Constant} \quad (11)$$

where  $r$  is radius and  $l$  is length of the cylinder and where  $A$  is characteristic coefficient of the cylinder. Correspondingly, parabolic and circular curves are found. This characteristic coefficient derivation for the mesh-tube can be described geometrically. If we uncurl the cylinder to a rectangle, the diagonal length should be constant for the meshed tube structure constraints:  $(\text{Diagonal length})^2 = 4\pi^2 r^2 + l^2 = \text{Constant}$ , which can be simplified as (11).

#### B. Locomotion Mechanism

The mesh-tube structure comprises multiple fibrillar spirals. Kinematically, each spiral is a stretched coil spring. The spirals cross each other in a diamond pattern and mathematically form a number of rhombi, as shown in Fig. 5(a) using cylindrical coordinates. The side lengths are assumed to be equal and remain constant during deformation, which follows (11). Each rhombus can contract in the tube longitudinal axis and bend out of plane along its diagonal, normal to the longitudinal axis. In Fig. 5(a),  $e$  remains constant and the radii of mesh crossing points ( $r_i, r_{i+1}$ ) changes depending on the deformation. Also,  $\theta$  in this case remains constant since the number of mesh crossing points along the perimeter is constant. The shape of the mesh can be uniquely determined by the calculation of the angle  $\beta_i$  as follows:

$$\beta_i = \cos^{-1} \left( \frac{\sqrt{r_{i+1}^2 + r_i^2 - 2r_{i+1}r_i \cos \theta}}{e} \right). \quad (12)$$

Once the radius profile is known as a function of  $\beta_i$  for each mesh crossing point  $i$ , the geometrical configuration of the entire mesh structure is readily available. We experimentally verified the radius profile as the stress-strain analysis of the weave of the elastic strands becomes excessively complicated.

The deformation of the mesh-tube structure is simulated by a numerical model in Fig. 5(b). Sequential radial contraction of multiple segments of the mesh-tube induces peristalsis as shown in Fig. 5(c) for robust locomotion. In this figure, solid red lines represent the body deformation in several time sequences between the first and second contractions. The dotted blue line indicates the trajectory of a point on the tube that contacts the ground periodically when segments contract radially.

On a flat surface, radial contractions cause the contact point to release from the ground and swing forward. Thus, a traveling wave is created by the trajectories of multiple points along the tube. This resembles locomotion in small anthropoids, which create multiple waves of leg trajectories instead of body deformation. The trajectories of points of a single segment depend on their position relative to the segment border. Assuming the segments are small enough, a pseudocontinuous wave of body deformation is created, where every point detaches from the

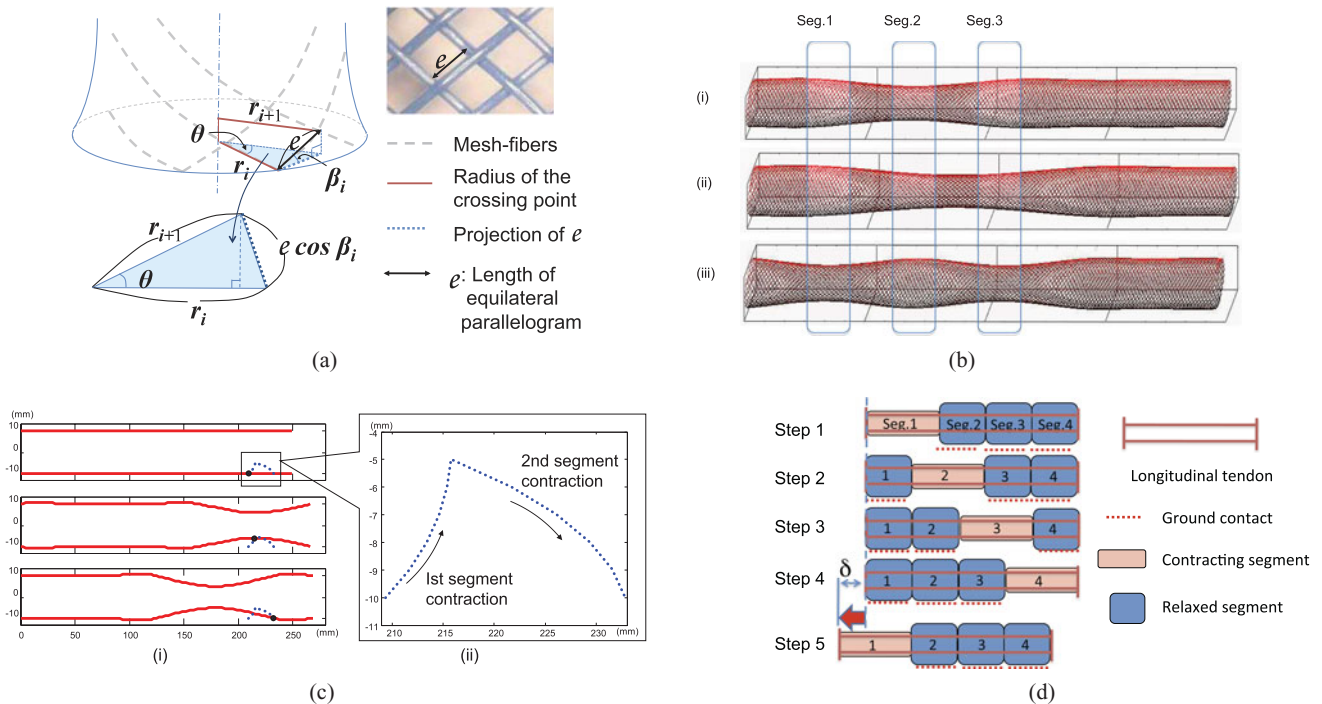


Fig. 5. Meshworm locomotion mechanism. The projection of an individual fiber in the mesh structure to the plane perpendicular to the axis of the mesh-tube. (a) The length of a spiral strand does not change over antagonistic deformation but changes in radius and height. (b) Simulation results of three actuation instances are displayed: (i) second segment is actuated, (ii) second and third segments are actuated, and (iii) first and third segments are actuated. (c) Simulation of the mesh-tube deformation (red solid lines) is shown in (i) the sagittal plane, and (ii) trajectory of a point on the tube is magnified. (d) Example of a peristaltic locomotion sequence by induced antagonism in the sagittal plane. The dotted red line represents contact with the ground. Longitudinal tendons keep the body length constant. Contraction of radial actuators induces radial expansion of adjacent segments.

ground, swings forward, and lands ahead of the initial contact point. Numerical simulation results show how a peristaltic wave is created by the radial and longitudinal actuators operating antagonistically to achieve effective locomotion without legs.

Two different arrangements of NiTi coils were considered for a mesh-tube worm robot. The first method consists of active antagonistic segments with both radial and longitudinal actuators. In this case, each segment can independently contract in radial or longitudinal directions allowing direct control of the state of each segment for various gaits. This arrangement, however, introduces complexities in fabrication and in synchronization across multiple NiTi actuators. The sensitivity of NiTi to heat dissipation makes it particularly challenging to synchronize multiple actuators in order to operate in phase for effective locomotion gaits.

The second method consists of induced antagonistic segments with only radial actuators. Flexible but inextensible tendons are attached along the body to replace longitudinal actuators at each segment. The tendons keep the total body length constant and couple the deformation of each segment in the longitudinal direction. Therefore, as the radial actuators of a given segment contract, the length of the segment expands and this leads to the longitudinal contraction of the remaining segments. Fig. 5(d) shows how the length constraint enables coupled behavior among segments. Consider the transition between the bottom two rows in Fig. 5(d). The radial actuators in the first segment (1) contract radially and expand in the longitudinal direction. The total length constraint by the tendons causes the

last segment (4) to contract longitudinally, and the robot crawls one step forward. This arrangement induces the necessary antagonism between the deformation in longitudinal and radial directions without a passive spring return. Section III-C describes a prototype soft mobile robot utilizing this second method.

In a study of peristaltic locomotion in earthworms, Quillin describes the locomotion speed by protrusion and stance times with stride length [7]. His analysis includes the total length change of the worms. Assuming the number of body segments is large enough, as is the case for natural worms, a general depiction of every possible gait using this approach yields a theoretical linear locomotion speed given as follows:

$$v = \delta \times N_w \times l_w \times f \quad (13)$$

where  $\delta$  is the length change of each segment,  $N_w$  is number of waves of contraction,  $l_w$  is a number of segments contracted in single wave, and  $f$  is the frequency of the waves.

### C. Experimental Investigation of Locomotion Gaits

To test and measure the effectiveness of several locomotion gaits for the Meshworm robot, we developed a gait controller based on LabVIEW software and an NI Single-Board RIO (NI sbRIO-9642). Various sequences of actuation, the number of segments, and duration can be rapidly assigned and tested using this tool.

An experimental prototype Meshworm, which incorporates the induced antagonism described in the previous section, was

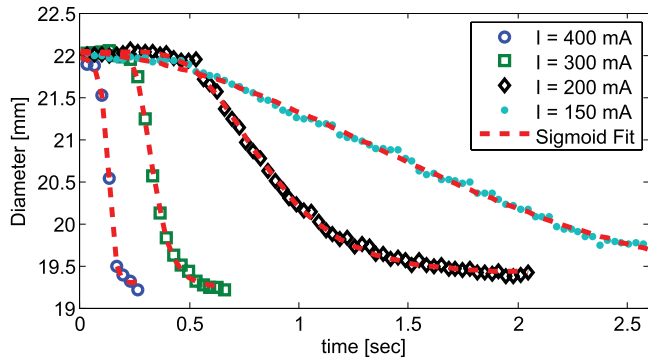


Fig. 6. Radius of the mesh as a function of time in different current settings on circumferential actuators.

built using a polyether ether ketone (PEEK) braided mesh tube. The tube was approximately 22 mm in diameter and each strand was 0.25 mm in diameter. The length of the tube was approximately 200 mm in the unloaded state. The unloaded state was created by annealing the PEEK mesh-tube around a metal pipe with the desired diameter. The annealing temperature was approximately 125 °C held for 10 min. Since PEEK is a thermoplastic, the unloaded state can be reconfigurable with different metal pipe sizes.

NiTi coils introduced in Section II and [4] were used for actuation. The wire diameter was  $d = 100 \mu\text{m}$  and the coil diameter was  $D = 400 \mu\text{m}$ . These parameters maintain a spring index of 4 from (6). The desired contraction of the mesh-tube diameter is 10 mm starting from the relaxed initial diameter of 20 mm. Using a thin flexible string wound around the mesh five times, the tension force required to contract the mesh-tube was measured to be 432.5 mN. The total string length in contact with the mesh-tube was 305 mm in the relaxed state and 261 mm at the desired contraction.

These numbers indicate that from Fig. 1,  $X_{A0} + \delta_h = 261 \text{ mm}$  and  $X_{M0} = 305 \text{ mm}$ . The number of active coils in the spring is given as  $n = X_{A0}/d$ . From (2), using the manufacturer's specification of the shear modulus for the SMA wire in austenite state as  $G_A = 31.125 \text{ GPa}$ , the given coil parameters yield  $X_{A0} = 152.5 \text{ mm}$  and  $\delta_h = 108.5 \text{ mm}$ . Choosing the actual SMA coil length of  $X_{A0} = 152 \text{ mm}$  in the austenite state, the value of  $X_{M0}$  was 317 mm, which was 3.94% greater than the desired  $X_{M0}$  of 305 mm.

Five NiTi actuators were wrapped around the tube in a helical pattern, creating five segments. Hence, the contraction of each actuator in length was translated to the radial contraction of each respective segment. The actuators are electrically driven by Joule heating. Fig. 6 displays a comparison of the radial deformation responses of a single segment under NiTi coil actuation with various current settings.

Since shape memory actuation is a thermal process, these actuators are typically rather inefficient. Efficiency can be improved by rapid large pulses of current, in comparison to longer small current signals [24]. A large current heats up the actuator much faster, and prevents the constant rate heat dissipation to the environment from wasting a lot of energy [24]. From Fig. 6,

TABLE I  
PARAMETERS OF THE INVESTIGATED LOCOMOTION GAITS

Gait	Current [mA]	$N_w$	$l_w$	Frequency [Hz]	Speed [mm/sec]
Short-Wave Mode	400	1	1	0.4	5.25
Long-Wave Mode	400	1	2	0.2	0.469

we can see this effect in practice. In these curves, a 200-mA current input fully contracts the segment in about 2 s, while a 400 mA current input contracts in approximately 0.25 s. For this larger current, the electrical energy supplied to this coil from Joule heating is about half of the value for a 200 mA input. Since both current inputs result in the same amount of mechanical work, pulsing a larger current is more energy efficient. This high current value, however, yields a steady-state temperature above the glass transition temperature of the body material and hence, should be applied for short time intervals only. The given pulse consumes about 3.2 J of energy.

We performed experiments to measure the total displacement and locomotion speed of the Meshworm and the length change of its segments. Color markers are placed at the borders of each segment for motion tracking and an external camera system (Microsoft LifeCam VX-3000) is used to capture the motion of the prototype. During Meshworm locomotion, the position of each marker is tracked using color segmentation. The distance between the markers indicates the segment length, and the position of the first marker determines the head position of the body. The frame rate is 15 f/s with  $640 \times 480$  resolution for locomotion experiments and 30 f/s with  $320 \times 240$  resolution for contraction experiments. The current applied to the actuators is 400 mA for 200 ms duration.

For locomotion experiments, we focus on single-wave gaits, since we found that the distance between multiple waves on the Meshworm prototype is not long enough to satisfy the cooling time requirements. Therefore, on the five-segmented Meshworm, actuating segments that have not properly cooled down leads to reduced contraction and inefficient locomotion. Two different locomotion gaits, whose parameters are listed in Table I, are tested. The first gait is the short-wave mode (SWM), where a single contraction wave is created along the length of the body ( $N_w = 1$ ) and one segment contracts at a time ( $l_w = 1$ ). The second gait is the long-wave mode (LWM), where a single wave ( $N_w = 1$ ) of two-segment contraction ( $l_w = 2$ ) is used. The frequency difference between the two gaits is due to cooling period differences. In SWM, we found that a cooling period of 2.3 s is enough. In LWM, this value has to be increased to 3.6 s as each segment is actuated for two steps in this mode.

Fig. 7(a) displays the segment lengths of the Meshworm during locomotion with the SWM. This figure indicates that the deformation is not repeatable between segments. This is a general issue of custom-made NiTi coil actuators due to small variations in the fabrication and assembly, and will be addressed in Section IV. Fig. 7(c) displays the overall displacement of the robot with the SWM. During the contraction of middle segment, there occurs some backward slippage, which is mainly due to friction and can be reduced by using a longer robot.

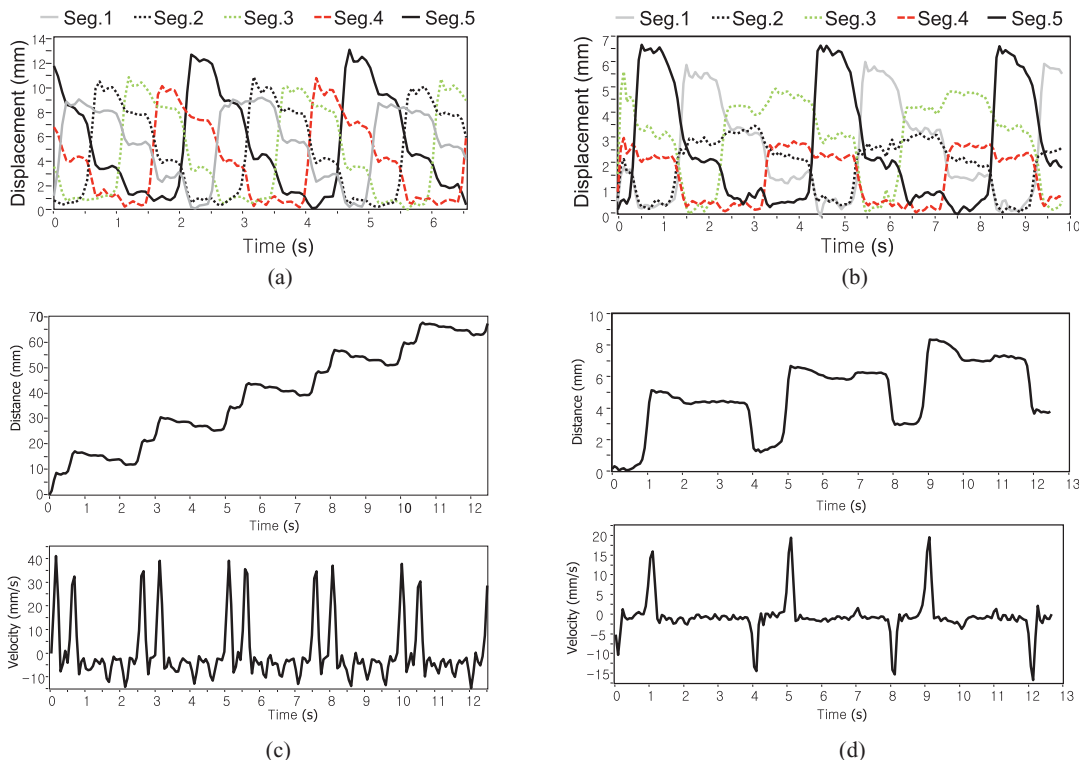


Fig. 7. Experimental results of locomotion gaits. Two different gaits were tested: SWM contracts one segment at a time and LWM has two segments contracted at a time. (a) Lengths of segments is shown as a function of time using SWM. (b) Displacement (top) and velocity (bottom) of the prototype using SWM. (c) Segment lengths are plotted as a function of time using LWM. (d) Displacement (top) and velocity (bottom) of the prototype using LWM. The data are filtered at 5 Hz.

From (13), an average segment deformation  $\delta$  value of 10.02 mm, a frequency  $f$  of 0.4 Hz, and  $N_w = l_w = 1$ , the theoretical locomotion speed is 4.08 mm/s. From the displacement plot in Fig. 7(c), the actual speed of the robot is measured as 5.25 mm/s which is larger than the theoretical speed. This seems to be counterintuitive as the theoretical prediction on speed should not be lower than the experimental measurements considering frictional losses and backward slippage during actual robot locomotion. The reason for this disparity can be explained by Fig. 7(a) and (c). In Fig. 7(a), the first segment does not have enough time to cool down and keeps elongated even while the second segment is actuated. Consequently, in Fig. 7(c), the robot takes an additional step during the actuation of the second segment. The effective length of the traveling wave is then  $l_w \approx 2$ , yielding a speed prediction of about 8 mm/s.

Similarly, Fig. 7(b) and (d) display the individual segment lengths and the overall locomotion information of the robot for the LWM, respectively. The wave-frequency in this mode is halved to allow enough cooling time for the actuators. From these parameters, (13) seems to predict that the forward speed of the robot for the LWM should be the same as for the SWM. In practice, however, this mode yields a smaller overall locomotion speed for two reasons. First, the segment deformation  $\delta$  is reduced since the initial length of the robot does not allow two segments to deform together as much. And second, there occurs more backward slippage as there are only three segments making contact with the ground in this case. These issues indicate that the robot design needs to take the target locomotion gait

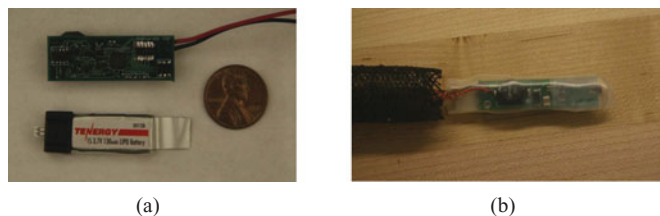


Fig. 8. Standalone implementation of the Meshworm. (a) Microcontroller prototype for gait generation and a compact Li-Poly battery. (b) Custom control board and a compact Li-Poly battery are covered by a heat-shrink tube and placed inside the robot body.

algorithm into consideration, by adjusting the radius and length of the robot for improved performance.

A standalone implementation of the Meshworm is achieved using a custom embedded control board. The control board shown in Fig. 8(a) has a very small form-factor to easily fit inside the robot body. Small LiPoly batteries supply the electrical energy to drive the robot. The PCB and the battery are wrapped in a heat-shrink tube and placed inside the robot body as shown in Fig. 8(b). The PCB is equipped with an ATmega88PA microcontroller and eight digital outputs to control eight MOSFET drivers using a separate actuation power line to protect the microcontroller from large currents and fluctuations. Actuation power is generated by an on-board step-up regulator. MOSFET drivers regulate power to individual NiTi coils to produce different gaits. The board also includes eight 10-bit A/D channels

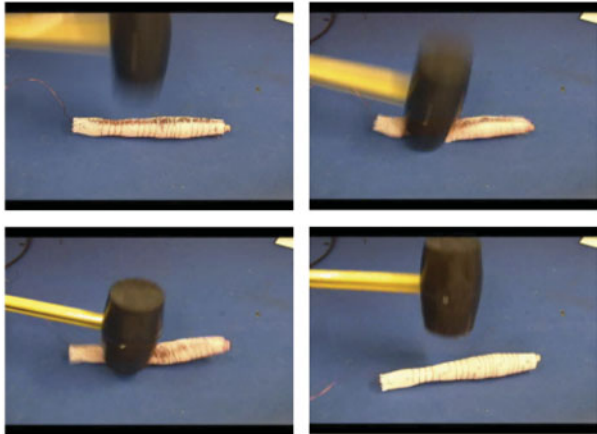


Fig. 9. Experiment to verify the robustness of the mesh-tube platform is performed. During locomotion, a rubber hammer impacts the mesh tube and the mesh tube experiences a substantial amount of impact on the body, but keeps functional.

toward a closed-loop implementation. Experiments with the embedded control board used the SWM. An average linear speed of 3 mm/s was measured with the standalone implementation. This speed decrease is due to the rigid PCB slightly constraining the segment deformation from the inside.

A key property of the robotic Meshworm is the inherent flexibility of the mesh-tube allowing a greater robustness of the structure. We rigorously tested this aspect of the robot by subjecting it to extreme conditions such as a hammer impact or a person stepping on it during operation. Fig. 9 displays snapshots of such an experiment. We found that the robot is robust enough to keep crawling after several impacts from the hammer.

#### IV. CONTROLLER DESIGN

Despite their many strengths, NiTi coils are sensitive to small changes in the environment and have repeatability issues between individual actuators. We use NiTi coils with large phase transition temperatures ( $90^\circ\text{C}$ ) to ensure that actuation is always on purpose. To force these actuators to work consistently among different segments and over time, we utilize feedback control.

Feedback control is useful to eliminate repeatability issues between individual segments and adapt to changes in the environment (e.g., wind, temperature), closing the loop with an appropriate sensor. To this end, we designed small sliding variable resistors as linear potentiometers to detect the length of each segment Fig. 10(a). When actuated, the length of a segment is detected by reading the corresponding resistance. A comparison of the readings of these embedded sensors to an external vision system, which tracks red markers on the body, is shown in Fig. 10(b). As seen in this figure, the difference between these two measurement systems is small, and more due to the size of the markers than the sliding resistors. The control board is designed to either supply current to a certain segment or not. Hence, the only control input we have in this system is the time interval of actuation.

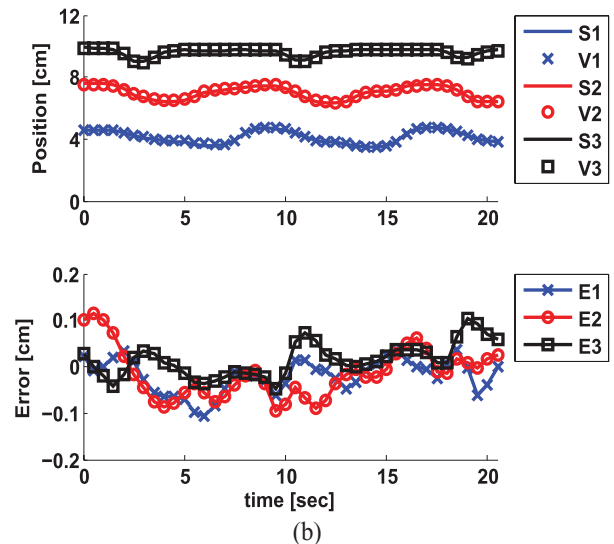
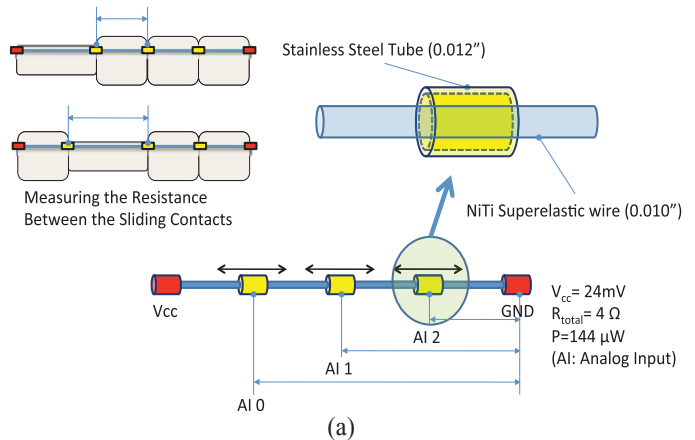


Fig. 10. (a) Linear potentiometer provides feedback. (b) Experimental analysis of embedded sliding resistors in comparison to an external vision system.  $S_i$  and  $V_i$  correspond to the measurements from the embedded sensors and the vision system, respectively, and  $E_i$  is the difference between the two measurements.

From Fig. 6, we experimentally determined that the deflection  $\delta$  of a single cell can be described by a general sigmoid function. The deflection of segments starts slowly in the beginning, picks up speed in the middle, and comes to a halt, where no discernible deformation occurs any more. In what follows, we will discuss four control schemes and compare their performances experimentally on a four-segment Meshworm robot prototype with embedded deflection sensors.

##### A. Open-Loop Control

For comparison, we will first give information about the open-loop control approach, using a fixed actuation time-step, which is the controller used in the previous sections. For a safe and repeatable experimental investigation, we set the fixed-time step as 2000 ms and added a 800 ms cooling period between actuation periods. This controller gives a forward speed of 0.495 mm/s at an average power of 3.783 W.

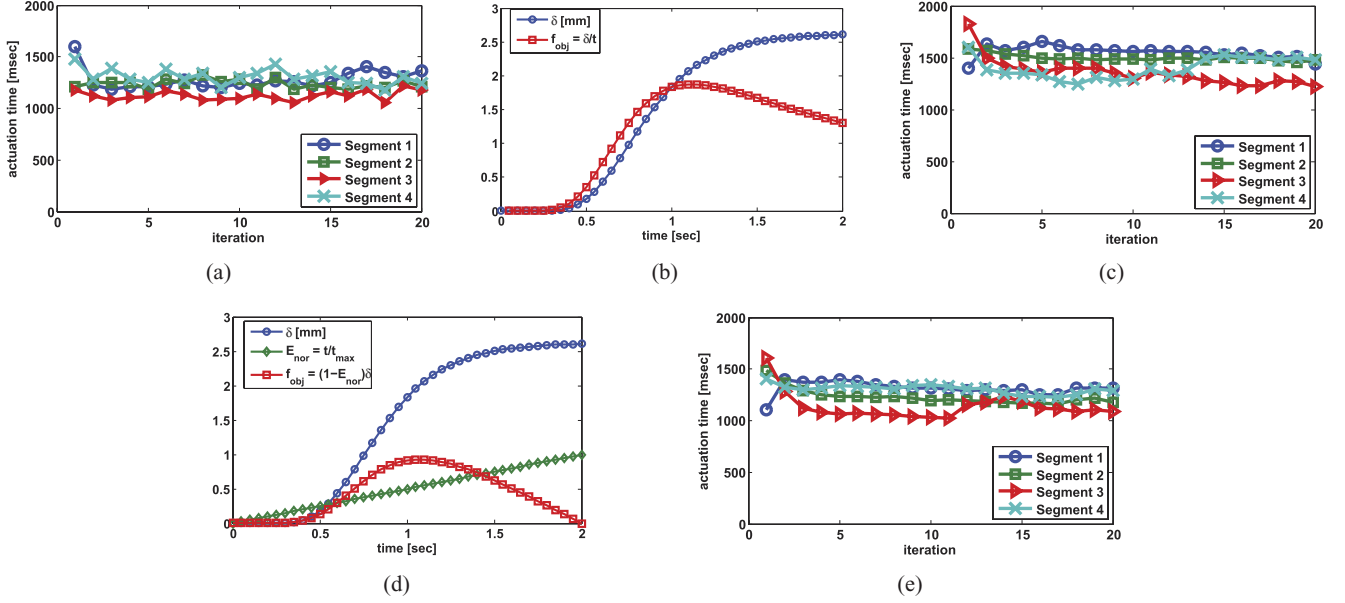


Fig. 11. Experimental results of various control algorithms. (a) Actuation time steps of each segment using a bang–bang controller. (b) Simulated deflection of a segment and the corresponding objective function to achieve maximum locomotion speed. (c) Actuation time steps of each segment using an ILC with an objective function to maximize speed. (d) Simulated deflection of a segment, the normalized energy function, and the corresponding objective function to achieve the joint optimization for maximum locomotion speed and minimum energy consumption. (e) Actuation time steps of each segment using an ILC with an objective function to maximize speed and minimize energy.

## B. Bang-bang Control

The simplest closed loop controller uses a bang-bang control algorithm. The controller turns a segment on, tracks the time response of deformation, and turns the segment off when no further deformation is registered. This controller uses four initial warm-up cycles using the maximum safe actuation time-step to calibrate its threshold values. During the initial deformations, the maximum and minimum deflection values are recorded from each segment and the turn-off threshold is set as 80% of the maximum deflection. The actuation time periods of each segment using this controller are displayed in Fig. 11(a). This controller gives a forward speed of 0.478 mm/s and an average power usage of 3.386 W with an average actuation period of 1250 ms.

## C. Iterative Learning Control

Since each segment of the Meshworm robot performs the same task in a repetitive manner, ILC is very suitable for this application. ILC works on the iteration axis, such that it uses information from past trials to correct its action, effectively learning from past performance [25], [26]. The controller updates the control input to optimize a given objective function  $f_{obj}$ , which defines its performance (e.g., minimize error). As mentioned, the control input in this case is the actuation period with a fixed current. The controller that maximizes the objective function is written as follows:

$$t_{i+1}^k = t_i^k + D \Delta f_{obj_i}^k \text{sgn}(\Delta t_i^k) \quad (14)$$

where  $t_i^k$  is the actuation period of segment  $k$  at iteration  $i$ ,  $D > 0$  is a tuning factor,  $\Delta f_{obj_i}^k = f_{obj_i}^k - f_{obj_{i-1}}^k$ , and  $\Delta t_i^k = t_i^k - t_{i-1}^k$ . As seen in this equation, the controller is similar to a

steepest descent algorithm. We analyze two different objective functions as follows.

1) *Maximum Speed*: To maximize the locomotion speed of the Meshworm, we set the objective function as:  $f_{obj} = \frac{\delta}{t}$ . This corresponds to a performance metric of average speed of deflection for each segment. Given a sample sigmoid function, this objective function takes the form shown in Fig. 11(b).

Using this metric, the actuation time periods of each segment are depicted in Fig. 11(c). This controller gives a forward speed of 0.506 mm/s and an average power usage of 3.525 W with an average actuation period of 1406 ms.

2) *Maximum Traveling Distance and Minimum Energy Consumption*: Energy efficiency is not one of the strengths of NiTi actuators. The previous objective function yields fast locomotion speeds at the expense of a large power consumption. Borrowing ideas from optimal control theory, here we design our objective function to penalize the effort (iteration time) while rewarding the deflection.

The energy consumption of a resistance under Joule heating is directly proportional to time ( $E = I^2 Rt$ ). Normalizing the energy with the energy consumed at the maximum iteration time ( $I^2 Rt_{max}$ ) yields  $E_{nor} = t/t_{max}$ . We combine this normalized energy consumption with the deflection  $\delta$  and arrive at an objective function written as:  $f_{obj} = (1 - E_{nor})\delta$ , which corresponds to a metric that defines the power consumption and deflection tradeoff. Hence, its maximization gives the joint optimization for the maximum deflection and minimum energy consumption. Given a sample sigmoid function, this objective function takes the form shown in Fig. 11(d). Note that, while we are giving equal importance to the speed and energy components here, this objective function can also be tuned by exponents added to each component according to specific importance factors.

TABLE II  
PERFORMANCE COMPARISON OF DIFFERENT CONTROLLERS FOR THE  
LOCOMOTION OF THE MESHWORM ROBOT

Method	Speed [mm/sec]	Average Power [W]	Actuation Period [msec]
Fixed Step	0.495	3.783	2000
Bang-bang	0.478	3.386	1250
Max. Speed ILC	<b>0.506</b>	3.525	1406
Max. Speed & Min.Energy ILC	0.444	<b>3.367</b>	1219

Using this metric, the actuation time periods of each segment are depicted in Fig. 11(e). This controller gives a forward speed of 0.444 mm/s and an average power usage of 3.367 W with an average actuation period of 1219 ms.

#### D. Comparison

The performance information for each controller presented in the previous sections are tabulated for ease of comparison in Table II. As seen in this table, the maximum speed and the minimum energy consumption are achieved by the first and second ILCs, respectively. The second ILC achieves the smallest locomotion speed to conserve energy. Fixed step open-loop control yields fast speed, but uses the most energy. Surprisingly, the simple bang-bang controller seems to make a good compromise between energy consumption and speed. Also, note that these values are slightly biased due to the existence of a constant finite cooling period between actuation steps, such that controllers that generate smaller actuation periods have a larger ratio of cooling period to actuation period, resulting in slower average speeds.

In light of these results, we identify the best usage scenarios of each of these controllers as follows. The open-loop fixed step controller is useful for sensor-less operation, for instance, in case a sensor fails during operation. The maximum speed ILC can be used during normal operation. In case, the robot is low on battery, it can switch to the second ILC to conserve power.

As mentioned, bang-bang controller represents a good balance of energy consumption and locomotion speed, but it has to be used with caution. This controller is not adaptive. In case of a failure that disables the contraction of a segment, bang-bang controller will keep trying to contract the segment, and possibly damage the actuator.

Note that the parameters we used for these experiments are found by trial and error. The actuation and cooling times for the fixed step controller are found from NiTi manufacturer specifications. The bang-bang cutoff deformation is found by the observation that the coil keeps deforming after the current is shut OFF. Iterative learning coefficient is manually tuned and kept constant for both ILC controllers for comparability.

#### V. STEERING

With the locomotion gaits discussed in the previous section, the Meshworm can crawl in a straight trajectory. In order to incorporate steering capabilities, we added two longitudinal muscles that replace two of the passive tendons in the design as shown in Fig. 12(a). Made of the same NiTi coil spring actuators, these muscles can actively change the length of one side

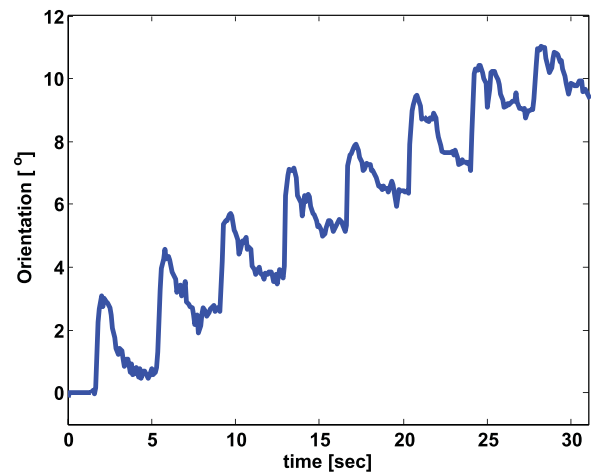
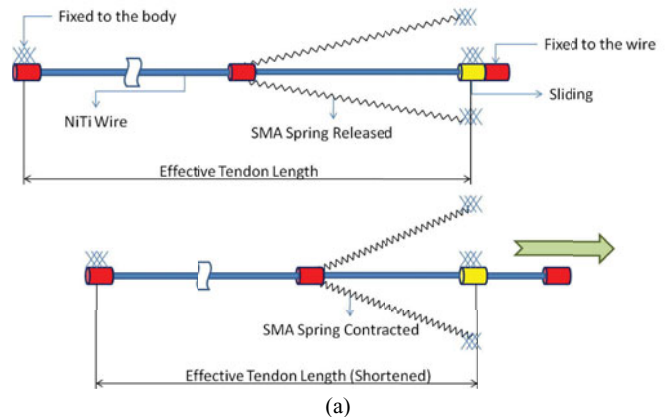


Fig. 12. (a) Steering of the Meshworm is achieved by longitudinal muscles. (b) Snapshots of the Meshworm steering right are displayed. (c) Orientation of the Meshworm changes over time due to the length difference.

of the robot to induce a rotational bias to the locomotion direction. Note that the robot design allows for the addition of more longitudinal muscles to achieve out-of-plane bending of the body, if necessary. For simplicity, we are focusing on the motion of the robot on a planar surface in 2-D using two steering actuators.

The contraction of one of the steering muscles transforms the motion axis by creating a uniform bending curvature of the body. Therefore, assuming no side-slippage, the robot is constrained to follow the arc created by its own body. Given the radius of curvature  $\rho$ , the angular speed of the robot is written using the

linear speed on the arc from (13) as

$$\omega = \frac{v}{\rho}. \quad (15)$$

Snapshots of a steering experiment of the Meshworm are depicted in Fig. 12(b). As apparent from these snapshots, some side-slippage occurs due to the lack of friction normal to the body axis, but this does not have an effect on the shape of the robot.

Using image processing of the video frames, we extract the orientation of the robot, defined as the average slope of the body with respect to an inertial reference frame, by color tracking red markers placed at each segment as seen in Fig. 12(c). We used a high-speed camera (Mikrotron MC1363) and a frame grabber (NI PCIe-1429) for the following motion tracking experiments for greater temporal resolution. We measure the average slope by fitting a line to the detected marker positions. As expected, major changes in the orientation coincide with the contraction of the first segment, which is also responsible for the forward motion, discussed in the previous section.

## VI. DISCUSSION

This study demonstrated a multisegmented soft robotic platform called the Meshworm, which can undergo peristaltic locomotion using NiTi coil spring actuators. Using the inherent antagonism of a soft braided-mesh body, which is constrained to keep its length constant, the robot propels itself by sending a traveling contraction wave over its segments. A complete analysis of the robot is presented from the theoretical modeling and experimental characterization of NiTi coil actuators to the investigation of different controllers for optimal performance.

An accurate model of NiTi spring actuators is developed that includes the change in free length of the spring due to phase transformation. By this model, NiTi coils can be precisely designed according to force and displacement requirements. This expands the potential for NiTi coil actuators beyond the scope of this study. Traditionally, actuators need gears or transmission mechanisms to match the impedance of the load, which makes the actuation system bulky. NiTi coils, however, can be tuned to match the load by changing the shape and the annealing temperature of the spring.

The mesh-tube prototype has less than ten segments, whereas its biological counterparts have close to a hundred segments. The length of each segment in the mesh-tube is longer compared to that of an earthworm. This prevents traveling waves from forming and limits the choice of gaits. The current manufacturing process involves manual construction and connections of the NiTi actuators to the mesh structure. More monolithic fabrication methods will enable a greater number of segments in a given length, and hence smoother waves and more efficient gaits. Since the platform contains no rigid components that may fail by external impact, this prototype can open a new space of applications for robust morphable robots.

With further development of a microprocessor and battery with flexible form factors, this approach suggests a new paradigm of completely soft robotics that can demonstrate significant body morphing and versatile locomotion capabilities.

While this is not our focus, an entirely compliant version of our system can be achieved with two changes. First, using flexible circuit boards the rigidity of the control system can be reduced. Second, many small batteries can be used together to make a flexible electrical power system. This is possible, since batteries technically do not need to have a specific size or shape.

Adding sliding resistors as linear potentiometers over the length of the robot, we achieved the ability to sense the deflection of segments. These sensors allowed us to develop closed-loop controllers. We designed, experimentally analyzed and compared four suitable control algorithms to enable faster speed and lower energy consumption.

Using two longitudinal muscles on two sides of the Meshworm body, we incorporated steering capabilities to the mobile robot. With the addition of multiple longitudinal muscles distributed along the circumference, the robot can operate in three dimensions to overcome large obstacles and traverse rough terrain.

## REFERENCES

- [1] W. M. K. D. Trivedi, C. D. Rahn, and I. D. Walker, "Soft robotics: Biological inspiration, state of the art, and future research," *Appl. Bionics Biomechanics*, vol. 5, no. 3, pp. 99–117, 2008.
- [2] C. D. Onal, X. Chen, G. M. Whitesides, and D. Rus, "Soft mobile robots with on-board chemical pressure generation," in *Proc. Int. Symp. Robot. Res.*, 2011.
- [3] Y. Sugiyama and S. Hirai, "Crawling and jumping of deformable soft robot," in *IEEE Int. Conf. Intell. Robots Syst.*, 2004, pp. 3276–3281.
- [4] S. Kim, E. Hawkes, K. Cho, M. Jolda, J. Foley, and R. Wood, "Micro artificial muscle fiber using NiTi spring for soft robotics," in *Proc. 2009 IEEE/RSJ Int. Conf. Intell. Robots Syst.*, 2009, pp. 2228–2234.
- [5] S. Seok, C. D. Onal, R. Wood, D. Rus, and S. Kim, "Peristaltic locomotion with antagonistic actuators in soft robotics," in *Proc. IEEE Int. Conf. Robot. Autom.*, 2010, pp. 1228–1233.
- [6] B. Kim, M. Lee, Y. Lee, Y. Kim, and G. Lee, "An earthworm-like micro robot using shape memory alloy actuator," *Sens. Actuators A, Phys.*, vol. 125, no. 2, pp. 429–437, 2006.
- [7] K. J. Quillin, "Kinematic scaling of locomotion by hydrostatic animals: Ontogeny of peristaltic crawling by the earthworm *lumbricus terrestris*," *J. Exp. Biol.*, vol. 202, pp. 661–674, 1999.
- [8] T. Nakamura and T. Iwanaga, "Locomotion strategy for a peristaltic crawling robot in a 2-dimensional space," in *Proc. IEEE Int. Conf. Robot. Autom.*, 2008, pp. 238–243.
- [9] N. Saga and T. Nakamura, "Development of a peristaltic crawling robot using magnetic fluid on the basis of the locomotion mechanism of the earthworm," *Smart Mater. Struct.*, vol. 13, no. 3, pp. 566–569, 2004.
- [10] J. B. A. B. Slatkin and W. Grundfest, "The development of a robotic endoscope," in *Proc. IEEE Int. Conf. Intell. Robot. Syst., Piscataway*, 1995, pp. 162–171.
- [11] E. Mangan, D. Kingsley, R. Quinn, and H. Chiel, "Development of a peristaltic endoscope," in *Proc. IEEE Int. Conf. Robot. Autom.*, 2002, vol. 1, pp. 347–352.
- [12] B. Kim, S. Park, C. Jee, and S. Yoon, "An earthworm-like locomotive mechanism for capsule endoscopes," in *Proc. IEEE Int. Conf. Intell. Robots Syst.*, 2005, pp. 2997–3002.
- [13] A. Menciassi, S. Gorini, G. Pernorio, and P. Dario, "A SMA actuated artificial earthworm," in *Proc. IEEE Int. Conf. Robot. Autom.*, 2004, vol. 4, pp. 3282–3287.
- [14] H. J. C. A. S. Boxerbaum and R. D. Quinn, "A new theory and methods for creating peristaltic motion in a robotic platform," in *Proc. IEEE Int. Conf. Robot. Autom.*, 2010, pp. 1221–1227.
- [15] M. Dolce and D. Cardone, "Mechanical behaviour of shape memory alloys for seismic applications—1. Martensite and austenite NiTi bars subjected to torsion," *Int. J. Mech. Sci.*, vol. 43, pp. 2631–2656, Nov. 2001.
- [16] B. Chang, J. Shaw, and M. Iadicola, "Thermodynamics of shape memory alloy wire: Modeling, experiments, and application," *Continuum Mech. Thermodyn.*, vol. 18, no. 1, pp. 83–118, 2006.
- [17] H. J. Lee and J. J. Lee, "Evaluation of the characteristics of a shape memory alloy spring actuator," *Smart Mater. Struct.*, vol. 9, no. 6, pp. 817–823, 2000.

- [18] Y. Dong, Z. Boming, and L. Jun, "A changeable aerofoil actuated by shape memory alloy springs," *Mater. Sci. Eng. A*, vol. 485, no. 1–2, pp. 243–250, 2008.
- [19] K. Cho, E. Hawkes, C. Quinn, and R. Wood, "Design, fabrication and analysis of a body-caudal fin propulsion system for a microrobotic fish," in *Proc. IEEE Int. Conf. Robot. Autom.*, 2008, pp. 706–711.
- [20] Y. Liu, "Detwinning process and its anisotropy in shape memory alloys," *Proc. SPIE Smart Mater.*, vol. 4234, pp. 82–93, 2001.
- [21] K. Otsuka and C. M. Wayman, *Shape Memory Materials*. Cambridge, U.K.: Cambridge Univ. Press, 1998.
- [22] G. Chapman, "Of the movement of worms," *J. Exp. Biol.*, vol. 27, pp. 29–39, 1950.
- [23] G. E. Newell, "The role of the coelomic fluid in the movements of earthworms," *J. Exp. Biol.*, vol. 27, pp. 110–122, 1950.
- [24] C. Zanotti, P. Giuliani, A. Tuissi, S. Arnaboldi, and R. Casati, "Response of NiTi SMA wire electrically heated," in *Proc. 8th Int. Symp. Martensitic Transformations*, 2009, no. 06037.
- [25] H.-S. Ahn, K. L. Moore, and Y. Chen, *Iterative Learning Control*. London, U.K.: Springer, 2007.
- [26] D. A. Bristow, M. Tharayil, and A. G. Alleyne, "A survey of iterative learning control: A learning-based method for high-performance tracking control," *IEEE Control Syst. Mag.*, vol. 26, no. 3, pp. 96–114, Jun. 2006.



**Sangok Seok** received the B.S. and M.S. degrees from the School of Mechanical and Aerospace Engineering, Seoul National University, Seoul, Korea, in 2002 and 2004, respectively. He is currently working toward the Ph.D. degree in the Biomimetic Robotics Laboratory, Department of Mechanical Engineering, Massachusetts Institute of Technology, Cambridge.

He was with the Korean branch of National Instruments as an Applications Engineer and a Marketing Engineer from 2004 to 2009. His research interests include the locomotion of soft body robotics and fast

running quadruped robots.



**Cagdas Denizel Onal** (S'06–M'10) received the B.Sc. and M.Sc. degrees from the Mechatronics Engineering Program, Sabanci University, Istanbul, Turkey, in 2003 and 2005, respectively, and the Ph.D. degree in mechanical engineering from Carnegie Mellon University, Pittsburgh, PA, in 2009.

He is currently a Postdoctoral Associate in the Computer Science and Artificial Intelligence Laboratory, Massachusetts Institute of Technology, Cambridge, focusing on flexible robots. He was engaged in vision-based control of a mobile robot and bilateral

control using sliding-mode controllers at Sabanci University. He was involved in automated and teleoperated micro/nanomanipulation at Carnegie Mellon University. He is the coauthor of a textbook on nanorobotics, based on his dissertation work. His research interests include soft robotics, printable robotics, alternative actuation/sensing mechanisms, bioinspiration, control theory, and micro/nanoscale and technology.



**Kyu-Jin Cho** (M'08) received the B.S and M.S. degrees from Seoul National University, Seoul, Korea, in 1998 and 2000, respectively, and the Ph.D. degree in mechanical engineering from the Massachusetts Institute of Technology, Cambridge, in 2007.

He was a Postdoctoral Fellow at the Harvard Microrobotics Laboratory until 2008. He is currently an Assistant Professor in the School of Mechanical and Aerospace Engineering and the Director of Biorobotics Laboratory at Seoul National University. His research interests include biologically inspired

robotics, robotics systems using smart actuators, novel mechanisms using smart structures, and rehabilitation and assistive robotics.



**Robert J. Wood** received the Master's and Ph.D. degrees in electrical engineering from the University of California, Berkeley, in 2001 and 2004, respectively.

He is currently an Associate Professor in the School of Engineering and Applied Sciences and the Wyss Institute for Biologically Inspired Engineering at Harvard University, Cambridge, MA. His research interests include the areas of microrobotics and bio-inspired robotics.



**Daniela Rus** (F'10) received the Ph.D. degree in computer science from Cornell University, Ithaca, NY.

She is a Professor of electrical engineering and computer science and the Director of the Computer Science and Artificial Intelligence Laboratory at the Massachusetts Institute of Technology (MIT), Cambridge. Before receiving her appointment at MIT, she was a Professor in the Computer Science Department at Dartmouth College, where she founded and directed two laboratories in robotics and mobile computing.

Her research interests include distributed robotics and mobile computing and her application focus includes transportation, security, environmental modeling and monitoring, underwater exploration, and agriculture.

Dr. Rus was the recipient of an NSF Career Award and an Alfred P. Sloan Foundation Fellowship. She is a Class of 2002 MacArthur Fellow and a Fellow of AAAI.



**Sangbae Kim** received the B.S. degree from Yonsei University, Seoul, Korea, in 2001, and the M.S. and Ph.D. degrees from Stanford University, Stanford, CA, in 2004 and 2008, respectively, all in mechanical engineering.

He is the Director of the Biomimetic Robotics Laboratory and an Assistant Professor of mechanical engineering at the Massachusetts Institute of Technology (MIT), Cambridge. He is involved in the convergence of mechanical engineering, control, biology, and material science. His research focuses on design

process extracting principles from complex biological systems to achieve legged locomotion in engineering. He is currently focusing on cheetah inspired robotic platform capable of high-speed gallop, employing principles from quadrupedal runners. His achievement on bioinspired technology development includes the world's first directional adhesive based on gecko lizards, and a climbing robot, Stickybot, that utilizes the directional adhesives to climb smooth surfaces. Stickybot was featured as one of the best inventions of 2006 by TIME magazine, and the papers on Stickybot won the best paper award for the Transactions on Robotics 2008 and IEEE International Conference on Robotics and Automation 2007.